Author Contributions:

Conceptualization: L. Deike
Data curation: L. Deike, B. G. Reichl
Formal analysis: L. Deike
Funding acquisition: L. Deike
Investigation: L. Deike, F. Paulot
Methodology: L. Deike, B. G. Reichl, F. Paulot
Project Administration: L. Deike
Software: B. G. Reichl
Writing – original draft: L. Deike
Writing – review & editing: L. Deike, B. G. Reichl, F. Paulot

A Mechanistic Sea Spray Generation Function Based on the Sea State and the Physics of Bubble Bursting

L. Deike[1,2], **B. G. Reichl[3]**, and **F. Paulot[3]**

[1]Department of Mechanical and Aerospace Engineering, Princeton University, Princeton, NJ, USA, [2]High Meadows Environmental Institute, Princeton University, Princeton, NJ, USA, [3]NOAA Geophysical Fluid Dynamics Laboratory, Princeton, NJ, USA

Abstract Bubbles bursting at the ocean surface are an important source of ocean-spray aerosol, with implications on radiative and cloud processes. Yet, very large uncertainties exist on the role of key physical controlling parameters, including wind speed, sea state and water temperature. We propose a mechanistic sea spray generation function that is based on the physics of bubble bursting. The number and mean droplet radius of jet and film drops is described by scaling laws derived from individual bubble bursting laboratory and numerical experiments, as a function of the bubble radius and the water physico-chemical properties (viscosity, density and surface tension, all functions of temperature), with drops radii at production from 0.1 to 500 µm. Next, we integrate over the bubble size distribution entrained by breaking waves. Finally, the sea spray generation function is obtained by considering the volume flux of entrained bubbles due to breaking waves in the field constrained by the third moment of the breaking distribution (akin to the whitecap coverage). This mechanistic approach naturally integrates the role of wind and waves via the breaking distribution and entrained air flux, and a sensitivity to temperature via individual bubble bursting mechanisms. The resulting sea spray generation function has not been tuned or adjusted to match any existing data sets, in terms of magnitude of sea salt emissions and recently observed temperature dependencies. The remarkable coherence between the model and observations of sea salt emissions therefore strongly supports the mechanistic approach and the resulting sea spray generation function.

Plain Language Summary Very large uncertainties in sea spray aerosol predictions remain despite long standing efforts, and play a critical role in large scale atmospheric processes, from radiative balance to life cycle of clouds. The uncertainties are related to the large range of scales involved, and the complexity of the original production processes, and lead to open questions on the dependencies on wind speed, ocean wave properties and water temperature. We propose a mechanistic formulation for sea spray aerosol emissions caused by bubble bursting at the ocean surface, by combining knowledge of individual bubble bursting processes, bubble statistics under breaking waves, and the distribution of breaking waves forced by realistic winds. The resulting sea spray aerosols emissions are in remarkable agreement with field observations, without being adjusted to match any existing data sets, in terms of magnitude of sea salt emissions and size distribution. The remarkable coherence between the model and observations of sea salt emissions therefore strongly supports the mechanistic approach and paves the way for improved modeling of atmospheric processes controlled by aerosols of oceanic origin.

1. Introduction

Knowledge of the size distribution of primary ocean spray aerosol particles and its dependence on meteorological and environmental variables is necessary for modeling cloud microphysical properties and the influence of aerosol on radiative processes (de Leeuw et al., 2011). Currently, the extent and brightness of marine low clouds are poorly represented in Earth system models, and the response of low clouds to changes in atmospheric greenhouse gases and aerosols remains a major source of uncertainty in earth system projections (de Leeuw et al., 2011; Painemal et al., 2015). Biases and uncertainties in predicting sea spray aerosols are expected to be particularly important in modeling remote regions, where perturbations by anthropogenic aerosols are limited (DeMott et al., 2016).

Sea spray aerosols are composed of small liquid droplets formed through two main pathways following wave breaking. The spume drops, produced from the tearing of breaking wave crests by strong winds, consist mostly of drops
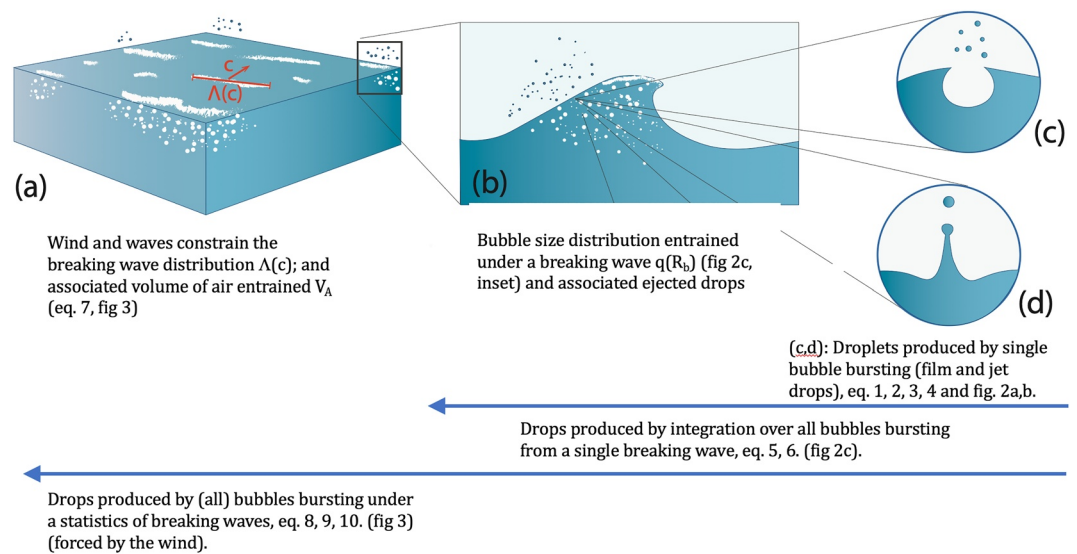
Figure 1. Sketch of the modeling approach, adapted from Deike (2022). Sea spray droplet mechanisms are presented in Section 2.1, with scaling relationships for the number and radius of ejected film and jet drops at production. The resulting sea spray size distribution produced by a breaking wave is then obtained by integrating over the canonical bubble size distribution in Section 2.2. Air entrainment by the wavefield forced by wind is then obtained by integration over the breaking distribution in Section 3. The resulting sea state sea spray generation function is then analyzed globally using a spectral wave model (Section 4).

larger than 10 μm (Veron, 2015). Drops produced by bursting bubbles are known as film drops (Blanchard, 1963; Lhuissier & Villermaux, 2012) and jet drops (Deike et al., 2018; Ghabache et al., 2014; Spiel, 1994, 1997), with radii at formation ranging from sub-microns to hundreds of microns. These droplets may be transported to the upper atmosphere (Richter et al., 2019), where they evaporate, and may serve as cloud condensation nuclei (de Leeuw et al., 2011; Lewis & Schwartz, 2004). The droplets can transport dissolved gases, salts, and biological materials, with their chemical composition affected by the production mechanisms (Bertram et al., 2018; Cochran et al., 2017; Prather et al., 2013; Quinn et al., 2015; X. Wang et al., 2017).

Large uncertainties remain in predicting the sea spray aerosol size generation functions. Numerous parameterizations of sea spray production have been proposed with very large uncertainties and variability of several orders of magnitude through the full spectrum of droplet radii (de Leeuw et al., 2011; Gong, 2003; Lewis & Schwartz, 2004; Mårtensson et al., 2003; Meskhidze et al., 2013; Ovadnevaite et al., 2014; Veron, 2015). As a consequence, predictions for the total amount of sea salt emitted over the ocean vary by a factor of 50 (de Leeuw et al., 2011). Once implemented in atmospheric models as sources of sea spray aerosols, the particular choice of parameterization will affect the modeled radiative budget through direct and indirect effects contributing to uncertainties on the precise role of sea salt aerosols on atmospheric processes, as well as their potential impact on climate (Johnson et al., 2020; Paulot et al., 2020). In particular, the sensitivity of sea spray aerosol emissions to temperature remains uncertain and is not well characterized (Cochran et al., 2017; Forestieri et al., 2018; Liu et al., 2021; Salter et al., 2014; Sellegri et al., 2006; J. Wang et al., 2021) which prevents a proper assessment of the potential role of sea spray aerosol in a warming climate (Johnson et al., 2020; Paulot et al., 2020).

The lack of quantitative representation of the production processes leads to tuning of multiple empirical coefficients in order for the sea spray generation function, to match observations. In contrast, we propose a mechanistic approach leading to a sea state dependent sea spray generation function from bubble bursting, summarized in Figure 1. Our model combines a physical description of air entrainment and bubble size distribution under breaking waves, together with a statistical description of the droplets being ejected by bubble bursting at the air-sea interface. We consider drop production by film drops and jet drops. The radius and number of drops ejected for a given bubble size distribution is characterized based on extensive laboratory and numerical studies of the individual bursting mechanisms, and physically accounts for variations in bubble radius, and variations in water density, viscosity, surface tension and temperature. The breaking distribution is characterized according to the distribution of length of breaking crest that physically accounts for the role of the sea state through the surface

wind-wave spectrum. Our approach does not require tuning of parameters to obtain a particular wind or temperature dependence as these physically arise from the modeling steps at various scales. The obtained size distribution is determined by the bursting mechanism with a sensitivity to temperature in terms of the radii and number of drops produced, while the wind sensitivity arises from the dependence of the total amount of air being entrained by breaking waves on the local wind and waves.

Section 2 summarizes the mechanisms for droplet production by individual bubbles and the associated physical scaling relationships derived from fundamental studies (theory and laboratory). Section 3 integrates the bursting mechanisms into a generation function, by considering the size distribution of bubbles created by breaking waves and the breaking wave distribution, and we discuss the resulting spectral (size) dependencies of the generation function. Section 4 applies the formulation globally by using a spectral wave model, forced by realistic winds, and global sea surface temperature data base, and we discuss the production of sea salt globally. Section 5 presents a discussion on the accuracy of the proposed approach, remaining uncertainties, and potential for practical use of sea-state dependent air-sea fluxes formulations.

2. Mechanisms of Droplet Production by Bubble Bursting

Droplets are produced by bubble bursting through a variety of mechanisms, with physical descriptions that remain an active research topic. Two mechanisms are considered here that encompass the full range of drop production and are described in detail below: film bursting leading to film drops, and cavity collapse leading to jet drops, sketched in Figure 1. The drops have radii at formation ranging from sub-micron to super-micron depending on the bubble radius. Laboratory and numerical studies provide a detailed description of the number and radius of drops formed by a single bursting bubble for the separate mechanisms, together with the range of applicability in terms of bubble radius and liquid properties (viscosity, surface tension). We summarize in this section and in Figure 1 our current mechanistic knowledge of drop production by bubble bursting, based on laboratory experiments and numerical simulations for jet and film drops performed on individual bubbles (see Deike, 2022, for a recent summary).

Our discussion on the droplet production process by bubble bursting yields predictions for the drop radius at formation (or 98% relative humidity by convention (Lewis & Schwartz, 2004)). These droplets are transported and evaporate in the surrounding atmosphere, so that the literature reports data in terms of the droplet radius at 80% relative humidity $r_d^{80\%}$ and the salt (dry) particle diameter D_{dry}. The conversion factor between dry solid salt particles and droplets radius is taken as $2D_{dry} = 2r_d^{80\%} = r_d$ (see Fitzgerald, 1975; Lewis & Schwartz, 2004). We note the recent revision on the sea salt hygroscopicity (Zieger et al., 2017). Section 2 presents results on the numbers n and radii r_d of drops at formation formed by bursting bubbles (consistent with the fluid dynamics literature e.g., Berny et al., 2021; Lhuissier & Villermaux, 2012). In Sections 3 and 4, we use the above conversion factor and present the results in terms of D_{dry} or $r_d^{80\%}$ (in-line with most of the literature on sea salt aerosols e.g., de Leeuw et al., 2011; Lewis & Schwartz, 2004). Note that below $D_{dry} \sim 0.1$ μm, the sea spray aerosols are mainly of organic composition (Bertram et al., 2018; Quinn et al., 2015), and their radii is not directly proportional to the liquid drop radius as opposed to that for sea salt aerosols.

2.1. Number and Mean Droplet Radius Produced by Bubble Bursting

2.1.1. Jet Drops

Jet drops are produced when the bubble cavity collapses and forms a vertical upward jet that destabilizes into drops. Berny et al. (2021) (following Berny et al. [2020]) used large ensembles of numerical simulations to describe the statistics of jet drop ejection, characterizing the number and radius of all jet drops being produced; evaluated against laboratory data (Brasz et al., 2018; Ghabache & Séon, 2016; Ghabache et al., 2014; Spiel, 1994, 1997), see also Lewis and Schwartz (2004), Hayami and Toba (1958), Blanchard and Woodcock (1957), Moore and Mason (1954), and Blanchard (1963, 1989). The data are well described by physical scaling relationships initially derived by Gañán-Calvo (2017). Jet drops are produced by bubbles with radius R_b smaller than the capillary size, $R_b < \ell_c$, with $\ell_c = \sqrt{\gamma/\rho g}$, ρ the water density, g acceleration due to gravity, and γ the air-water surface tension. The smallest bubble able to produce a jet drop is determined by a visco-capillary balance. Experiments and simulations suggest $R_{b,\min}/l_\mu \approx 900$ (Berny et al., 2020; Walls et al., 2015), with $l_\mu = \mu^2/\gamma\rho$ the visco-capillary length (μ the water dynamic viscosity), which at 20°C corresponds to $R_{b,\min}$ close to 10 μm. While bubbles of 10 μm radius

are able to produce (sub)micron drops, the presence of bubbles of 10 μm at the ocean surface remains uncertain. Bubbles of radii from 10 to 50 μm have rise velocity of a few mm/s, and might fully dissolve before they reach the surface (Lewis & Schwartz, 2004). Note that if the rise velocity is too small compared to the typical water turbulent velocity fluctuations, the bubbles would act as flow tracer and never reach the surface; while any bubbles will be slowed down by the turbulence fluctuations. The radius of the smallest bubble at the surface remains uncertain (as no direct measurement exists in the field) but is estimated here to be $R_b \approx 60$ μm based on dissolution (Lewis & Schwartz, 2004) and bubble dynamics in turbulence (Aliseda & Lasheras, 2011). The mean number and radius at ejection of jet drops follow Berny et al. (2021)

$$n_{jet}(R_b) = \chi_1(R_b/l_\mu)^{-1/3} \text{ and } \langle r_d \rangle_{jet} = \chi_2 l_\mu(R_b/l_\mu)^{5/4}, \tag{1}$$

with $\chi_1 = 145$ and $\chi_2 = 0.008$ non dimensional coefficients adjusted to the single bursting data. Smaller bubbles lead to more drops (due to the capillary wave selection process) and a maximum of about O(10) drops are ejected, and the mean radius from 0.5μ for a O(10 μm) bubble to 500 μm for a O(2 mm) bubble. We note that the number and size of emitted jet drops is sensitive to temperature through the water viscosity, which has been extensively tested experimentally and numerically (Berny et al., 2020; Brasz et al., 2018; Ghabache et al., 2014).

2.1.2. Film Drops

Film drops are generated by the rupture of the thin layer (film) of water that initially separates the bubble from the atmosphere. The droplet radius and number are controlled by the film thickness at bursting h_b. We consider two modes of production associated with film drops, following Lhuissier and Villermaux (2012) and Jiang et al. (2022) and using physical scaling relationships for the mean values of the number and radius of the ejected droplets based on various data sets.

The first mode of production (mode I in the following) is associated with a centrifuge process ejecting the film after bursting. Such film drops are produced by bubbles with radius $R_b \geq 0.2\ell_c$, corresponding to 0.6–10 mm in salt water, leading to drops with radii at formation ranging from 0.5 μm to several hundreds of μm (Blanchard & Syzdek, 1988; Cipriano & Blanchard, 1981; Lhuissier & Villermaux, 2012; Resch & Afeti, 1991). Lhuissier and Villermaux (2012) proposed a set of scaling relationships for the mean number and radius at ejection

$$n_{filmI}(R_b) = \chi_3(R_b/l_c)^2(R_b/h_b)^{7/8} \text{ and } \langle r_d \rangle_{filmI} = \chi_4 R_b^{3/8} h_b^{5/8}, \tag{2}$$

with $\chi_3 = 0.04$ and $\chi_4 = 0.5$, and h_b the mean film thickness at rupture, which varies from 0.1 to about 50 μm for bubbles from 1 to 10 mm, leading to drops in the same range of sizes. Lhuissier and Villermaux (2012) and Poulain et al. (2018) proposed that the film thickness at rupture is controlled by Marangoni stresses, originating from fluctuations in temperature and contamination at the water surface. These theoretical arguments lead to a dependency in a local Sc number, with $Sc = \nu/D$ a Schmidt number describing the diffusion of contaminant on the bubble surface, where D is the diffusivity of contaminant in the film (which can be obtained by Einstein's formula, $D = k_B T/(6\mu\pi r_c)$, where k_B is Boltzman constant, T the seawater temperature, and r_c the typical contaminant size). We note that the nature of contaminant is not considered here, and that surface elasticity effects that might reduce evaporation are neglected. This leads the semi-empirical scaling for film thickness at bursting, $h_b = \chi_5 Sc^{-1/2} R_b^2/l_c$ (Poulain et al., 2018; Shaw & Deike, 2022), with $\chi_5 = 0.04$. At relative humidity of 80%, the smallest mean film drop radius is $\approx r_d^{80} \approx 0.5\mu$m (using $r_d^{80\%} = 0.5 r_d$). The sensitivity to temperature for the film thickness at bursting has received some experimental confirmation (Poulain et al., 2018; Shaw & Deike, 2022), however the sensitivity of the size and number of film drops (Equation 2) to temperature remains to be fully validated experimentally.

Separately, numerous measurements have reported solid dry particles (sea salt aerosols) with diameters as small as 0.01 μm attributed to film drops (Cipriano & Blanchard, 1981; Mårtensson et al., 2003; Resch & Afeti, 1991; Sellegri et al., 2006; X. Wang et al., 2017), as summarized in Lewis and Schwartz (2004). These submicron film drops have recently been attributed to a flapping mechanism (Jiang et al., 2022) that applies for bubbles from about 100 μm to 1.2 mm in salt water. Combining the recent data from Jiang et al. (2022) and those summarized by Lewis and Schwartz (2004), we propose a set of empirical scaling relationships, leading to

$$n_{filmII}(R_b) = \chi_6 Sc^{-1/2}(R_b/l_c)^2 \text{ and } \langle r_d \rangle_{filmII} = \chi_7 Sc^{-1/2}(R_b/l_c)^{1/3}, \tag{3}$$
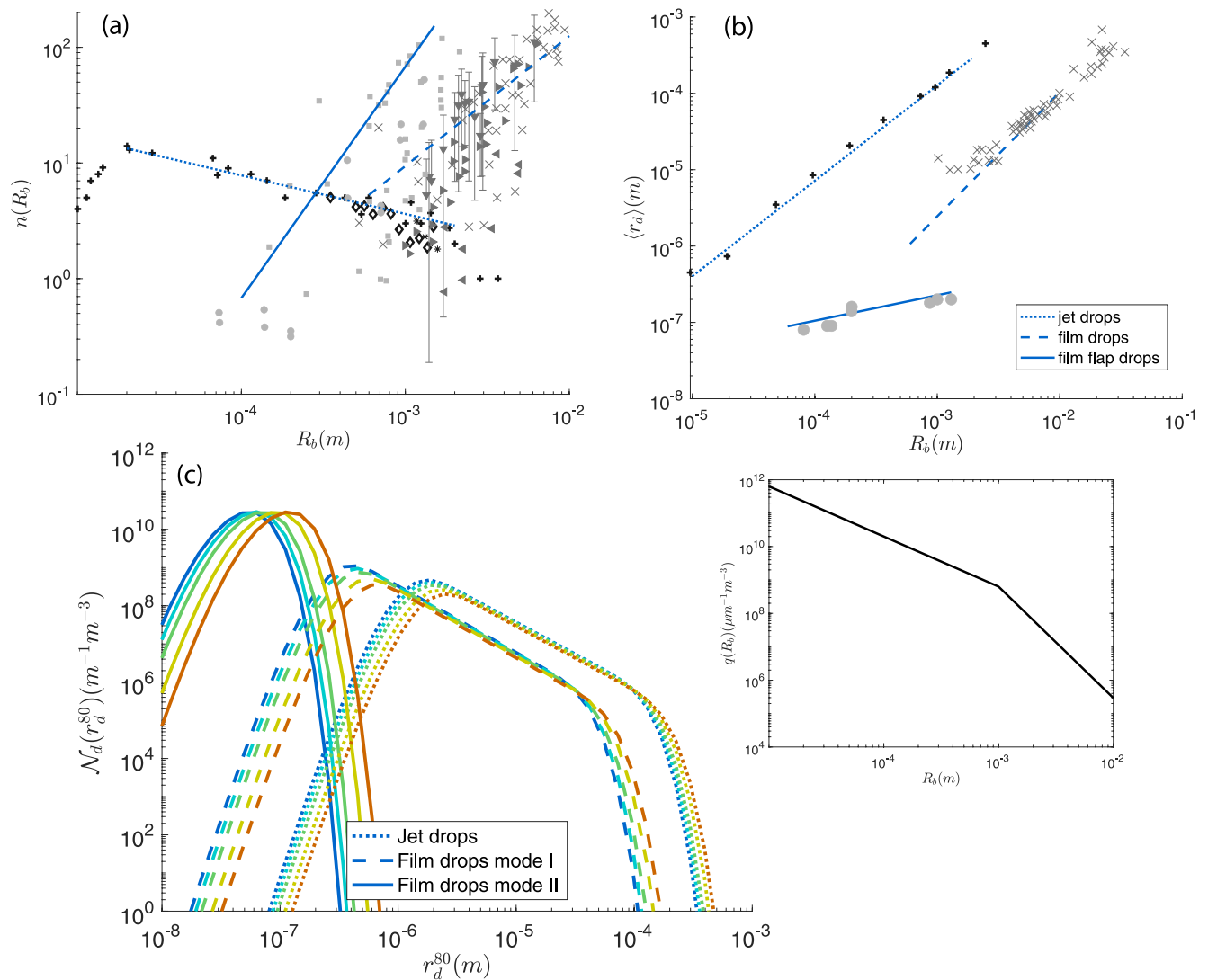
Figure 2. Summary of number $n(R_b)$ (a) and mean radius $\langle r_d \rangle$ (b) of ejected liquid droplets, as a function of the bursting bubble radius R_b, for jet drops (dotted lines), and film drops separated into two sub-processes (mode I, dashed lines and II, solid lines). For bubbles from 0.1 to 1 mm, film drops (mode II) produce up to O(100) droplets, with mean radius at formation around 0.1 μm. For bubbles above 1 mm, larger film drops (mode I) are produced (from 1 to 100 μm). Jet drops are produced from bubbles of O(20 μm) to a few mm, leading to radii from O(1 μm) to O(100 μm). Lines (dot, dash and solid) are the semi-empirical relationships at 20°C proposed to describe the data (Equations 1–3). Symbols are single bursting data. Black for jet drops, dark gray for film I, light gray film II. Black crosses (Berny et al., 2021); black diamonds (Spiel, 1998); black stars (Ghabache, 2015). Gray crosses (Lhuissier & Villermaux, 2012); Gray squares, compilation from Lewis and Schwartz (2004); gray dots and triangles (Jiang et al., 2022); Down gray triangles (Shaw & Deike, 2022). (c) Resulting droplet size distribution (Equation 5), after integration over the bubble size distribution ($q(R_b)$, show in inset). The droplet distribution $\mathcal{N}_d \left(r_d^{80} \right)$ is expressed in terms if the radius at 80% relative humidity, for film (mode I, dashed lines; and mode II solid lines) and jet drops (dotted lines). A bubble cut-off of 60 μm is considered (see text). Temperature is color coded from cold (blue) to warm (red) water, with values of 1, 5, 10, 20, and 30°C. Temperature sensitivity is described by the scaling relationships (Equations 1–3). More drops are produced for colder water for jet drops and large film drops, while the opposite trend appears for small film drops. The radius of the peak of production shifts to larger values with increasing temperature.

with $\chi_6 = 3.6 \times 10^6$ and $\chi_7 = 5 \times 10^{-5}$. The scaling follows the dependence on bubble radius suggested by the data from Jiang et al. (2022) and historical data summarized by Lewis and Schwartz (2004), with a reasonable agreement as shown in Figure 2. We note that the temperature dependency in terms of the Sc number is suggested from the scaling proposed in Jiang et al. (2022) and Poulain et al. (2018) and remains to be validated experimentally. These drops will be called film drop mode II, or flap drops.

Figure 2 summarizes the mean drop radius and mean number of ejected drops, together with data from the literature (Berny et al., 2021; Blanchard & Syzdek, 1988; Cipriano & Blanchard, 1981; Ghabache & Séon, 2016; Jiang et al., 2022; Lewis & Schwartz, 2004; Lhuissier & Villermaux, 2012; Resch & Afeti, 1991; Shaw & Deike, 2022;

Spiel, 1998), with the colored lines corresponding to temperature increasing from 1 (blue) to 30°C (red). The coefficients in the various scaling relationships (χ_i) are obtained from least squares fits to the experimental data. Uncertainties on the jet drop numbers are evaluated to be of less than a factor of 2 (Berny et al., 2021; X. Wang et al., 2017) and on the size of the drop of less than 30% (Berny et al., 2020, 2021; Gañán-Calvo, 2017). Uncertainties for film drops are larger due to the statistical variability in the bubble life time, which controls the film thickness at bursting. The film thickness itself controls the number and size of ejected drops (as visible in Figure 2a), such that the uncertainty is evaluated to be between a factor of 2–4.

For each of these three modes of production, the distribution of drop size production by bubble bursting is then be modeled by a Gamma distribution (Villermaux, 2020), a two-parameter function controlled by the mean drop radius $\langle r_d \rangle$ and its order m,

$$\mathcal{P}\left(r_d / \langle r_d \rangle\right) = \frac{m^m}{\Gamma(m)} \left(\frac{r_d}{\langle r_d \rangle}\right)^{m-1} e^{-m \frac{r_d}{\langle r_d \rangle}}. \tag{4}$$

The values of the order m considered here will be $m = 11$ for both film and jet drops (the order of the Gamma function will only affect the shape at the tail and peak of the distribution, with the cut-off length being the most important parameter). The adequacy of the Gamma distribution to describe film and jet drops distributions is discussed in Lhuissier and Villermaux (2012) (single bursting experiments on film drops), Berny et al. (2021) (numerical simulations on jet drops) and Neel et al. (2022) (collective bursting experiments on film and jet drops).

2.2. Bubble Size Distribution Under a Breaking Wave and Associated Sea Spray Droplet Distribution

We now construct the associated sea spray generation function due to bubble bursting. We assume a representative size distribution of bubbles entrained by breaking waves, based on laboratory and numerical studies. We assume that the associated bubbles that burst at the surface follow the same distribution (neglecting coalescence at the surface), and that the bursting process is well captured by the scaling relationships described in Section 2 (Equations 1–4). These assumptions could be modified by considering the bubble plume evolution and measurements of the surface bubble size distribution actually bursting, as discussed in Néel and Deike (2021) and Neel et al. (2022) on surface dynamics of an ensemble of bubbles and possible collective effects.

The bubble size distribution entrained by a breaking wave has received extensive scrutiny (Deike, 2022). Based on laboratory (Blenkinsopp & Chaplin, 2010; Deane & Stokes, 2002; Loewen & Melville, 1994; Rojas & Loewen, 2007) and numerical (Deike et al., 2016; Mostert et al., 2022; Rivière et al., 2021, 2022; Z. Wang et al., 2016) work, the size distribution can be described as following two power laws, above and below a critical length scale, the Hinze scale R_H (Hinze, 1955). The Hinze scale is the scale at which surface tension prevents fragmentation by turbulence and in ocean conditions, $R_H \approx 1$ mm (Deane & Stokes, 2002). The size distribution $q(R_b)$ of bubbles entrained under a breaking waves, and defined as the number of bubbles per bin size, per unit volume, follows $q(R_b) \propto R_b^{-10/3}$ for bubbles $R_b > R_H$, while $q(R_b) \propto R_b^{-3/2}$ for $R_b < R_H$ (Deane & Stokes, 2002; Mostert et al., 2022; Rivière et al., 2021, 2022; Z. Wang et al., 2016). The total number of entrained bubbles is constrained by the breaker geometry (wave slope and wave speed) and a balance between buoyancy and turbulence forces (Deike et al., 2016, 2017; Mostert et al., 2022). Uncertainties of the total number of bubbles entrained is evaluated to be of a factor of 2 (Deane & Stokes, 2002; Deike, 2022; Mostert et al., 2022). Field measurements of the bubble size distribution under breaking waves close to the water surface remain limited due to significant technical challenges (Czerski et al., 2022a, 2022b).

The size distribution of drops produced by bubble bursting entrained by a breaking wave can then be obtained by integration over all bubble radii (Berny et al., 2021; Deike, 2022; Lhuissier & Villermaux, 2012),

$$\mathcal{N}_d(r_d) = \int_{R_{b,\min}}^{R_{b,\max}} \frac{q(R_b) \, n(R_b)}{\langle r_d \rangle (R_b)} p(r_d / \langle r_d \rangle, R_b) \, \mathrm{d}R_b, \tag{5}$$

where $n(R_b)$, $\langle r_d \rangle$ are respectively the number and mean radius of drops resulting from one of the mode of production (jet, film mode I or mode II, subscripts have been omitted for simplicity), $R_{b,\min}$ and $R_{b,\max}$ are the lower and upper bound of production of drops through the considered mechanism. The product $q(R_b) n(R_b) \mathrm{d}R_b$ gives the

number of drops generated by bubbles with radii between R_b and $R_b + dR_b$. The total size distribution of drops will then be obtained by summing over the three modes of production.

Defining $\tilde{\alpha}$ and $\tilde{\beta}$ such that $q(R_b)\,n(R_b) \propto R_b^{-\tilde{\alpha}}$, $\langle r_d \rangle \propto R_b^{\tilde{\beta}}$, and $\zeta = (\tilde{\alpha} - 1)/\tilde{\beta}$, Equation 5 integrates to (Berny et al., 2021; Lhuissier & Villermaux, 2012)

$$\mathcal{N}_d(r_d) = \mathcal{A} r_d^{-1-\zeta} \left[\Gamma_{inc}(m + \zeta, m r_d/r_{d,\max}) - \Gamma_{inc}(m + \zeta, m r_d/r_{d,\min}) \right], \tag{6}$$

where Γ_{inc} is the incomplete Gamma function, $r_{d,\max} = \langle r_d \rangle (R_{b,\max})$, $r_{d,\min} = \langle r_d \rangle (R_{b,\min})$, and $\mathcal{A}$ is the combined pre-factor of the various algebraic laws.

For film drops (mode I), following Lhuissier and Villermaux (2012) we consider $R_{b,\min,filmI} \approx 0.6$ mm and $R_{b,\max,filmI} \approx 10$ mm, so that film drops are mostly produced by super-Hinze scale bubbles with $q(R_b) \propto R_b^{-10/3}$, hence $\zeta = 3/4$ so that $\mathcal{N}_d(r_d)_{film} \propto r_d^{-7/4}$. For film drops (mode II), following Jiang et al. (2022) we have mainly sub-Hinze bubbles (ranging from 0.1 to 1.2 mm), with $q(R_b) \propto R_b^{-3/2}$, hence $\zeta = -3/2$ so that $\mathcal{N}_d(r_d)_{filmII} \propto r_d^{1/2}$. For jet drops, following Berny et al. (2021), we consider $R_{b,\max,jet} \approx l_c \approx 2.7$ mm, so that jet drops are mainly produced by sub-Hinze bubbles, with $q(R_b) \propto R_b^{-3/2}$, hence $\zeta = 2/3$ so that $\mathcal{N}_d(r_d)_{jet} \propto r_d^{-5/3}$.

The coefficients $\mathcal{A}$ for each mechanism can be obtained by numerical integration of Equation 5 (with appropriate bounds and values of ζ). We obtain for jet drops, $\mathcal{A}_{jet} = A_J R_H^{5/3}$, with $A_J = 6.4 \cdot 10^4 (l_\mu/R_H)^{0.15}$; for film drops (mode I), $\mathcal{A}_{filmI} = A_{F,I} R_H^{7/4}$, with $A_{F,I} = 1.6 \times 10^8 Sc^{1/5}$; and for film drops (mode II), $\mathcal{A}_{filmII} = A_{F,II} R_H^{-1/2}$, with $A_{F,II} = 6.3 \times 10^{12} Sc^{-1/6}$.

The resulting droplet size distribution for the three modes of production are shown in Figure 2c, considering the canonical bubble size distribution (in number of bubbles per unit volume) under a breaking wave (shown in inset of Figure 2c). The bubble radius cut-off for drop production is chosen to be 60 μm, corresponding to bubbles rising at a few mm/s (Aliseda & Lasheras, 2011). We assume that bubbles with smaller rise velocity will be prevented from moving to the surface by turbulence fluctuations, similar to assumptions made when considering bubble dissolution (Deike, 2022; Thorpe, 1982; Woolf & Thorpe, 1991). The ejected droplet distribution is presented in terms of the radius at 80% humidity, r_d^{80} for consistency with the literature. The distributions for temperature increasing from 1 to 30°C (blue to red) are shown, and illustrate the role of temperature on the radius and total number of drops being ejected for the three modes of production. The number of film drops (mode II) is increasing with temperature, while the film drops mode I and jet drops number decrease with increasing temperature. For all modes of production, an increase in temperature leads to an increase in the diameter at which the distribution peaks. The film drops (mode I) coming from larger bubbles contribute to drops from 1 to several hundreds microns but are less numerous than the jet drops over the same range of conditions. For film mode I and jet drops, the asymptotic scaling $\propto r_d^{-7/4}$ and $\propto r_d^{-5/3}$ are observed, while the film-flap drop range of production is too narrow and appears mostly as a single peak or mode of production. The film-flap drops are the main source of sub-microns sea spray aerosols. We note that the smallest jet drops are highly sensitive to the cut-off chosen for the smallest bubble present in the system, here considered to be about 20 μm. If a different cut-off is chosen, for example, 10 μm (respectively 100 μm), then the smallest r_d^{80} obtained would be 0.5 μm (respectively 5 μm). This discussion highlights the importance of the choice of the bubble size distribution in the present framework, and we caution that direct measurements of the surface bubble size distribution in the field do not exist so that our understanding is entirely based on theoretical considerations and laboratory measurements.

3. A Sea State Dependent Sea Spray Source Function

In the open ocean, surface waves are primarily generated by the wind. At the onset of wind, the sea-state develops and the wind-sea wave age increases as a function of the time and distance (fetch) that the winds force the waves. Waves of longer wavelengths are energized through non-linear processes that transfer energy from shorter waves into much longer waves (wavelengths up to several hundreds of meters). These long waves, or ocean swell waves, then propagate freely through the open ocean, capable of transmitting energy to distant coasts. At a given time in the ocean, the local sea-state therefore reflects the combination of the locally generated waves that are highly correlated to the local wind, and remotely generated swell waves that are mostly independent of the local wind. A parameterization for the sea spray source function that is formed using only the wind speed cannot explicitly

capture the sea state dependent variability of local wave properties due to the remotely generated swells. We now describe a more comprehensive approach to capture the sea spray source function variability that considers the full wave spectrum.

3.1. Air Entrainment and Bubble Production by Breaking Waves

The classic approach to go from sea spray production by individual bubble bursting to ocean conditions has been to use the whitecap coverage as a proxy for the total amount of bubbles present at the ocean surface (de Leeuw et al., 2011; Lewis & Schwartz, 2004). The lack of a quantitative link between the whitecap coverage and the number of bubbles has then required some arbitrary fitting parameter, while the scatter in the whitecap coverage data adds to the overall uncertainty in the global constraints on the number of bubbles. Phillips (1985) introduced the length of breaking crest $\Lambda(c)$ moving at speed between c and $c + \mathrm{d}c$ as a way to quantify the breaking dynamics and the associated air-sea fluxes of mass, momentum and energy. The whitecap coverage can be related to the second moment of $\Lambda(c)$, $W \propto \int c^2 \Lambda(c) \mathrm{d}c$, as demonstrated by Kleiss and Melville (2010) using field measurements and Romero (2019) using spectral wave modeling.

In order to construct our sea spray generation function, we aim to consider a quantity directly related to the number of bubbles and integrate the canonical bubble size distribution under a breaking wave $q(R_b)$ for a given sea state and wind. Deike et al. (2017) showed that the bubble flux entrained is provided by the third moment of $\Lambda(c)$ for a given sea state and wind speed (and used in Deike and Melville [2018] to propose a sea state dependent bubble mediated gas transfer model). The volume of air entrained is constrained by laboratory experiments and direct numerical simulations (Deane & Stokes, 2002; Deike et al., 2016, 2017; Lamarre & Melville, 1991; Mostert et al., 2022) and Deike et al. (2017) defines the rate of entrainment of air per unit area of ocean surface, V_A (dimensions of a volume per area per time),

$$V_A = \int B s(k)^{3/2} \frac{c^3}{g} \Lambda(c) \, \mathrm{d}c, \tag{7}$$

where $s(k)$ is the wave slope, and $B = 0.1$ is a constant (Deike et al., 2016). The wave slope within a complex wavefield can be estimated from the wave spectrum $\phi(k)$, with k the wave number, linked to the wave speed by $c = \sqrt{g/k}$, and (following Romero et al. [2012] and Romero [2019]) we consider $b/hk = s(k)^{3/2} = A_T \left(\sqrt{k^3 \phi(k)} - \sqrt{B_T} \right)^{3/2}$ using the same constants A_T and B_T as for energy dissipation (Drazen et al., 2008; Romero et al., 2012). The volume flux V_A entrained by breaking waves is the volumetric analog of the whitecap coverage (Deike & Melville, 2018; Deike et al., 2017).

3.2. Air Entrainment From a Spectral Model

We evaluate the sea state dependent sea spray generation function by using a global spectral wave model (such as WAVEWATCH III, WW3, WW3DG, 2016), able to simulate the growth and propagation of wave energy in the wave spectrum $\phi(k)$ from atmospheric forcing (e.g., Ardhuin et al., 2010; Chawla et al., 2013; Janssen & Janssen, 2004; Komen et al., 1996). We utilize the breaking statistics model from Romero (2019) that relates the wave spectrum $\phi(k)$ to the breaking distribution $\Lambda(c)$. The wave properties in terms of wave spectrum peak period, significant wave height and wave spectrum shape have been extensively validated (Chawla et al., 2013). The breaking statistics model from Romero (2019) has been shown to be compatible with field measurements of $\Lambda(c)$ (from Sutherland and Melville [2013] and Zappa et al. [2012]): it retrieves the $\Lambda(c) \propto c^{-6}$ scaling from Phillips (1985), and leads to accurate energy dissipation by breaking, as well as classic whitecap coverage relationships (Romero, 2019).

We perform global WW3 simulations forced by the Japanese Meteorological Society Reanalysis product (JRA55-do), which provides ten-m wind vectors (U_{10}) at approximately half-degree resolution every 3 hours (Kobayashi et al., 2015; Tsujino et al., 2018). This approach follows closely to Reichl and Deike (2020), but extends the wave model spectral grid to match Romero (2019). We employ the wave model physics package ST4, which combines the wind-input source term consistent with Ardhuin et al. (2010) with the dissipation source term from Romero (2019). Inputs to the wave model include the three-hourly wind vectors and daily varying

sea-ice from a separate ocean sea-ice simulation (following Adcroft et al. [2019]). The methodology and resulting wavefield are consistent with previous results for modeling the gas transfer velocity (Deike & Melville, 2018; Reichl & Deike, 2020).

Snapshots of the wave and wind fields demonstrate significant spatial and temporal variability associated with atmospheric weather events (50–100 km of horizontal scale) that dominates instantaneous wind, wave, and air entrainment patterns, as discussed in Reichl and Deike (2020) and shown in Figures 3a (wind), 3b (significant wave height), and 3c (volume of air entrained V_A). The monthly means of these fields in January 2008 and July 2008, as representative example are shown in Supporting Information S1 and demonstrate how these events correspond to global wind and wave patterns and thus to the air entrainment and eventually sea spray emissions. Strong air entrainment is visible in regions of high wind and wave activities, namely higher latitude and winter seasons; which will correspond to the highest emission of sea spray. Importantly, the fact that the air entrainment needs both a strong wind and an active wavefield to reach high values leads to a more pronounce zonal variation, which will be of importance when considering annual budget of sea spray.

The whitecap coverage (W) can be estimated from the wave model following Romero (2019). A typical snapshot of the whitecap coverage output is shown in Figure 3d (small gray dots) and is compatible with existing recent data sets (within the spread of the observational data, and with similar trends with wind speed), also shown in Figure 3d (Bell et al., 2017; Brumer et al., 2017; A. Callaghan et al., 2008; Kleiss & Melville, 2010; Schwendeman & Thomson, 2015). As discussed in the literature, the mean of W for each data set can be described as a power of wind speed at 10 m, or some mixed wave-wind variable, but require empirical fitting of the coefficients (de Leeuw et al., 2011; Gong, 2003; Lewis & Schwartz, 2004; Mårtensson et al., 2003; Meskhidze et al., 2013; Ovadnevaite et al., 2014; Veron, 2015). Some of the variability in the whitecap coverage data at a given wind speed comes from variability in the sea state which is explicitly accounted in our approach, using a wave spectral model.

The sea state variability in air entrainment at a given wind speed is illustrated in Figure 3e which shows V_A computed using Equation 7 from a mechanistic understanding of the sea state as a function of wind speed. At each wind speed, a significant scatter is observed, corresponding to the variations in wave state (various wave history, fetch, etc). The volume of entrained air can be described on average by a power law of the wind speed in Figure 3e, analogous to the various scalings proposed for the whitecap coverage, setting $\langle V_A \rangle = 1.8 \cdot 10^{-7} (U_{10} - 5)^{2.5}$ (with the prefactors having the appropriate dimensions). However, significant sea state induced variability from the mean at a given wind speed is visible, which again is similar to the scatter in the whitecap coverage data. The whitecap coverage and the air entrained are directly linked as V_A is computed from the third moment of $\Lambda(c)$, while W is computed from the second moment (Romero, 2019) leading to an empirical relationship, $\langle V_A \rangle = 4 \times 10^{-3} W^{4/3}$ (shown in Supporting Information S1). As such the present framework could be applied using whitecap coverage data and translating the relationship with wind speed for V_A. We note that the exponent on wind speed is within the range of recent observation (see Figure 3d) but significantly smaller than the one originally proposed by Monahan and Muircheartaigh (1980) and used in several global models.

Figure 3f shows the annual mean in air entrainment, which highlights regions of strong wind and wave activities, where sea spray emissions will be important. We define the sea state induced variability by computing on each point (and at each time step) the difference between the local value and its mean value at the given wind speed, $\delta V_A = V_A - \langle V_A \rangle$. Figure 3g shows the annual mean variability induced by the sea state and demonstrates up to 30% added variability in mid to high latitude, corresponding to storm track location, similar to the discussion in Reichl and Deike (2020). Similar results are observed when considering seasonal averages (as shown in Supporting Information S1).

Lewis and Schwartz (2004) discuss the possible role of water temperature on air entrainment and whitecap coverage. A re-analysis of whitecap coverage measurements for temperature ranging from cold (below 4°C), intermediate (between 4 and 17°C) and warm (above 17°C) is presented with a weak increase in whitecap coverage within the noise of the data, concluding that no clear effect could be established. A. H. Callaghan et al. (2014) presents a similarly weak effect in a laboratory breaking-wave analog experiment. Here, we present a reanalysis of the data collected by Brumer et al. (2017) and Bell et al. (2017) during field campaigns in the North Atlantic, with systematic measurements of the whitecap coverage for water temperature varying from 4 to 20°C. Figure 3d shows the whitecap coverage color-coded by the sea surface temperature. We confirm the conclusion from Lewis and Schwartz (2004) that there is no noticeable effect of temperature on air entrainment by breaking waves in
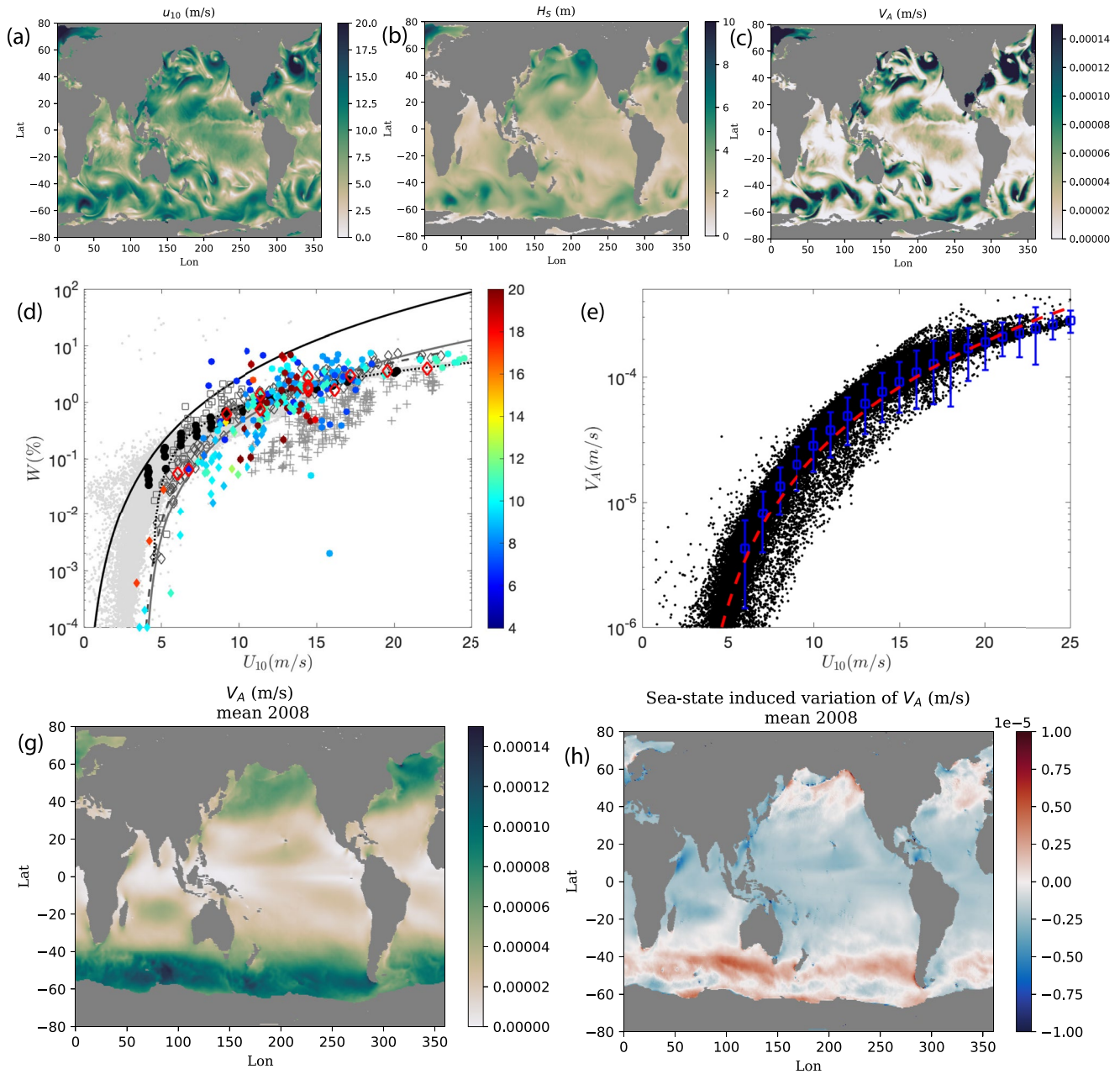
Figure 3. Global evaluation of entrained air V_A and the role of wind speed and sea state. First row: (a) Snapshot of wind speed, (b) significant wave height, and (c) entrained air V_A. Second row: (d): Whitecap coverage (W, a classic proxy for air entrainment) showing a general increase with wind speed, and significant scatter in the data. Sea surface temperature is color coded for some of the data and no clear influence is visible, so that W can be considered independent of temperature. Data with SST information are from Brumer et al. (2017) (dots) and Bell et al. (2017) (diamond), while gray markers are from Kleiss and Melville (2010) (crosses), A. Callaghan et al. (2008) (gray squares), and Schwendeman and Thomson (2015) (gray diamonds). Lines are fits with wind from Brumer et al. (2017) (gray dashed), A. Callaghan et al. (2008) (black dotted) Schwendeman and Thomson (2015) (gray dotted) and the historical fit from Monahan and Muircheartaigh (1980) (solid black line). Black dots are modeling from Romero (2019) and light gray dots are single snapshot data from our run. (e) Instantaneous V_A, computed from a snapshot as a function of wind speed. The mean trend can be fitted by $V_A = 1.5 \cdot 10^{-7}(U_{10} - 2.5)^{2.5}$ (red line, while blue markers are bin-averages; similar to the type of fits performed on the whitecap coverage. Third row: (f): annual average of V_A and (g) shows sea state induced variability.

3.3. Integration Over Breaking Statistics and Sea State Dependent Sea Spray Source Function

The distribution flux of bubbles under breaking waves is defined as the number per unit ocean surface area per unit time per unit bin size, $Q(R_b)$, related to the air volume flux V_A by $V_A = \int Q(R_b) 4\pi/3R_b^3 dR_b$. We use the distribution flux of bubbles to formulate a sea state dependent sea-spray source function resulting from bubble bursting, as proposed by Deike (2022), adapting the ideas proposed for bubble mediated gas transfer (Deike & Melville, 2018).

The sea-spray source function F_d, resulting from one of the bursting mechanisms and defined as number of drops per unit surface ocean area per unit time, the same dimensions as $Q(R_b)$, is given by

$$F_d(r_d) = \int Q(R_b) \frac{n(R_b)}{\langle r_d \rangle (R_b)} p\left(\frac{r_d}{\langle r_d \rangle}\right) dR_b. \tag{8}$$

The sea-spray generation function for each bursting mechanism can then be written in terms of the third moment of $\Lambda(c)$, the canonical bubble size distribution under a breaking wave $q(R_b)$ discussed in Section 2 (Figure 2), introducing a dimensional constant assuring volume consistency, $C_A q(R_b) = Q(R_b)$. This leads to the sea spray generation function, written as a double integral (over c and R_b) or the product of the volume flux and the drop production function,

$$
\begin{aligned}
F_d(r_d) &= \int \frac{B}{2\pi} \frac{s(k)^{3/2} c^3}{g} \Lambda(c) dc \int \frac{q(R_b)}{C_A} \frac{n(R_b)}{\langle r_d \rangle (R_b)} p\left(\frac{r_d}{\langle r_d \rangle}\right) dR_b, \\
F_d(r_d) &= \frac{V_A}{C_A} \mathcal{A} r_d^{-1-\zeta} \left[\Gamma_{inc}\left(m+\zeta, m\frac{r_d}{r_{d,\max}}\right) - \Gamma_{inc}\left(m+\zeta, m\frac{r_d}{r_{d,\min}}\right) \right],
\end{aligned}
\tag{9}
$$

with C_A insuring the volume is constrained by the third moment and dimensional consistency, while values of $\mathcal{A}$, ζ, m, and the bounds $r_{d,\max}$ and $r_{d,\min}$ determined for each mode of production (given in Section 2, and in Supporting Information S1).

The total sea spray generation function is then the sum of the three mechanisms, writing

$$\mathcal{F}(r_d) = \sum F_d(r_d). \tag{10}$$

The formulation explicitly considers the sea state effects through the $\Lambda(c)$ distribution and the slope spectrum $s(k)$, controlling the number flux of bubbles $Q(R_b)$ and the air entrainment V_A, as illustrated in Figures 3 and 4. Physico-chemical variables, such as temperature and viscosity, control the droplet production mechanism and are included within the drop production functions (which in the end results in the coefficients $\mathcal{A}$, ζ and the bounds of production). Rearrangements of bubbles at the surface due to coalescence and other collective bubble effects are not considered here, and we assume that the volume of air entrained and its associated size distribution will on average lead to production of drops following the individual mechanisms. Finally, there are uncertainties on each step of the model construction, but the scaling laws proposed and the coefficients used correspond to the best of our knowledge at this point. The proposed model leads to a consistent physics based formulation of sea spray aerosols.

4. Sea State Dependent Sea Spray Generation Function

4.1. Sea State Variability in a Single Storm

We now consider a typical winter storm in the Southern Ocean in Figure 4 (lat. 46° S, long. 318° E), as representative of storm high wind and wave conditions, which is used to illustrate the sea state effect on the sea spray emission. The wind speed over these 24 hr is shown (Figure 4a) together with the entrained air V_A (Figure 4b) and the sea spray emission function (Figure 4c). The wind increases from 5 to over 20 m/s in a few hours, with significant wave height going from 3 to 7 m (the resulting wave spectrum $\phi(k)$ and breaking statistics $\Lambda(c)$ are
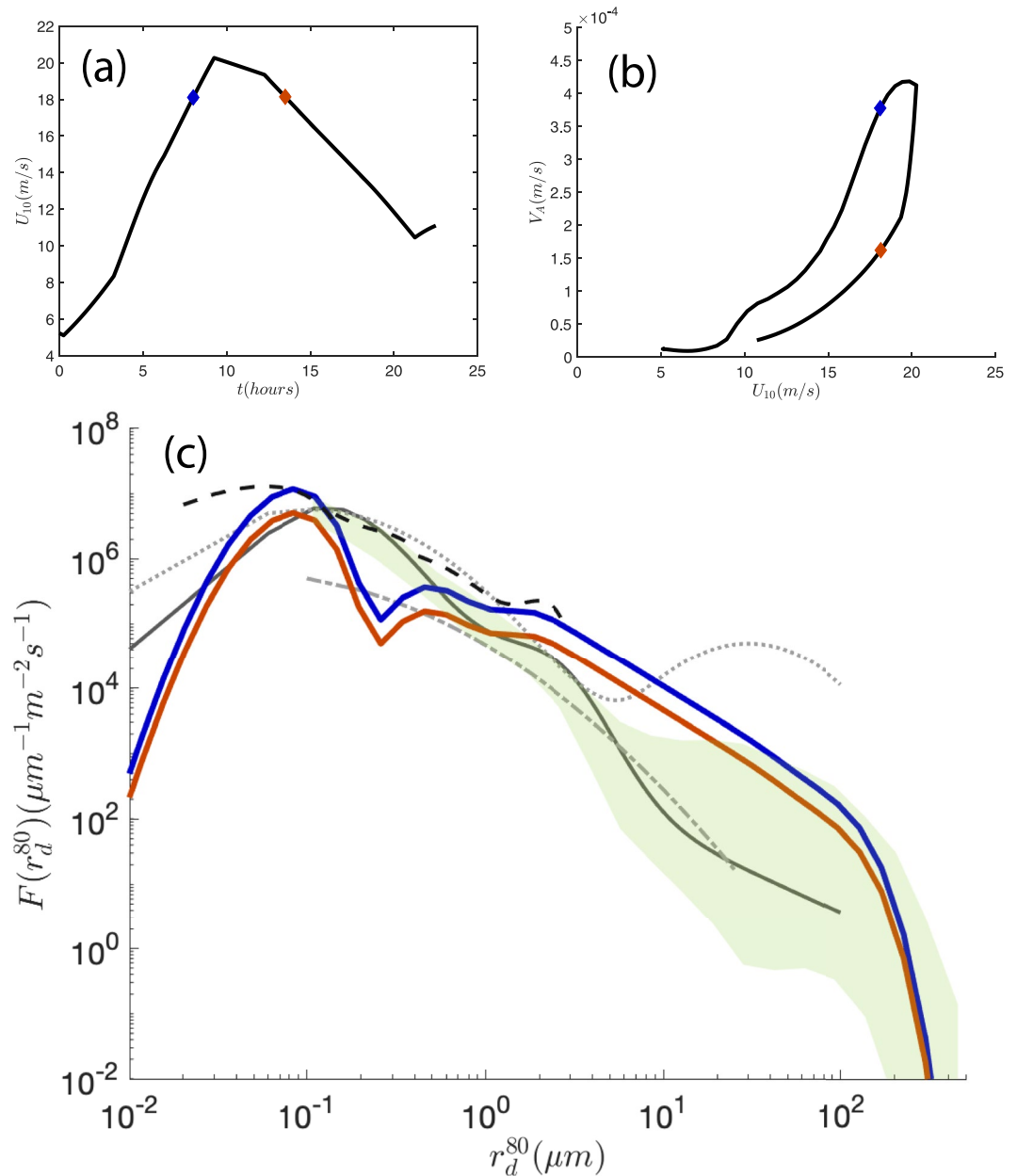
Figure 4. Sea spray generation function (SSGF) (Equation 8) during one storm in the Southern Ocean, simulated by WW3. SST is 10°C. (a) Wind speed as a function of time during the 24 hr period, increasing from 5 to 20 m/s over 10 hr, and then setting down. (b) Entrained air V_A computed using Equation 7 over the storm duration. A clear hysteresis cycle is observed with more air entrained during storm intensification, due to the local wavefield. The blue and red diamonds indicate times when wind speed reaches 18 m/s before and after the storm peak, respectively. (c) Resulting Sea Spray Generation Function from Equation 8. The lines correspond to the sum of the three components. Peaks around 100 nm correspond to the film drop mode II, slightly below 1 μm film drop mode I, and a peak around 2 μm corresponding to jet drop. The drop radius at equilibrium at 80% relative humidity is related to the radius at formation, $r_d^{80} = 0.5 r_d$. More drops are ejected during the storm intensification, corresponding to more intense breaking events, with the blue thick line being higher than the red thick line. Light green area indicate typical SSGF summarized by Veron (2015) at 15 m/s. The Sea Spray Generation Function at 18 m/s from Lewis and Schwartz (2004) (gray dash-dot line), Jaeglé et al. (2011) (gray solid line), Grythe et al. (2014) (light gray dotted line), and Mårtensson et al. (2003) (black dashed line). Our mechanistic sea state dependent formulation falls within the uncertainties of previous empirical data, and explains some of the variability previously reported.

shown in Supporting Information S1). The corresponding entrained air is shown, with a strong peak when the wind speed is maximum and the wave activity peaks.

The intensification and set down are asymmetric in terms of air entrainment. The asymmetry is related to a higher entrainment of air for young waves, leading to substantive difference in the breaking dynamics during the storm intensification compared to the set down of the wavefield. The resolution of such wave history effects obtained through direct computation of V_A via the wave spectrum further motivate the use of our sea state dependent formulation, compared to wind only formulation as it leads to variations in air entrainment (and thus droplet production). The hysteresis is illustrated in Figure 4b which shows the entrainment associated with a 18 m/s wind speed before (blue) and after (red) the storm peaks differ by about a factor of 4.

Figure 4c shows the integration of Equation 8 summing the three modes of production described in Section 2: film drop (mode I and mode II) and jet drops. Film drops (mode II) dominate the production of sub-micron aerosols, while jet drops dominate the overall drop production above 2 μm. As in Figure 1c, a cut-off of 60 μm has been chosen for droplet production of jet drops which affect this discussion. The resulting sea spray source function is fully compatible with typical functions used in the literature and reviewed in Lewis and Schwartz (2004), Veron (2015), de Leeuw et al. (2011), and more specifically those proposed by Mårtensson et al. (2003), Gong (2003), Jaeglé et al. (2011), and Grythe et al. (2014) indicated on the figure for the same wind of 18 m/s. We stress that our approach is mechanistic with the dependency in temperature, wind speed and sea state based on physical modeling, and that the final function is not fit to data, contrary to most approaches. For all three drop production mechanism, the production is higher (blue line) during the storm intensification than during the set-down (red line), for the same wind speed (here 18 m/s). This result follows the pattern observed on the intensity of the wave spectrum and breaking distribution that controls the volume flux of air. The observed differences at the same wind speed controlled by the sea state rationalizes some of the natural variability reported in existing field measurements.

We note an apparent underestimation of our formulation for $r_d^{80} < 0.05$ μm. That size range corresponds to mostly organic aerosol particles which are not accounted in our model (while they are indirectly considered in empirically based formulation which lump all types of aerosols). We also reiterate that our formulation does not account for spume drops, which are expected to contribute to the distribution for $r_d^{80} > 300$ μm.

4.2. Global Application of the Sea State Dependent Generation Function and Sea Salt Emissions

We now consider a global WW3 simulation and estimate the distribution of sea salt aerosols emissions, using our new formulation. We obtain the sea state fields and entrained air flux V_A over a representative year (2008, with results qualitatively consistent for other years) and discuss the resulting sea salt aerosol production.

The emission of sea salt is estimated following de Leeuw et al. (2011) and Lewis and Schwartz (2004). The salt mass is given by $m_{dry} = \rho_{ss} 4/3\pi \left(r_d^{80}/2 \right)^3$, with $\rho_{ss} = 1.22$ g/cm^3 the sea salt density. Temperature is estimated using the skin SST provided by the daily NOAA OI-SST product (Reynolds et al., 2007), which is used to compute the viscosity, density and surface tension of salt-water from tabulated relationships.

Figure 5a shows the annual emitted sea salt aerosols with diameter below 10 μm. Emissions peak in the North Atlantic and Southern Ocean due to high wind and wave activities. This pattern is similar to other parameterizations such as that of Grythe et al. (2014) (Figure 5b). Peaks of production are of a few hundreds of g/m^2/yr in high wind (and wave) regions. Integrating globally over the full year yields sea salt emissions of 15 Pg/yr, which is comparable to the estimate proposed by Grythe et al. (2014) (about 10 Pg/yr, while reviewing values for the literature ranging from 3 to 70 Pg/yr) and in the upper range of emissions summarized by de Leeuw et al. (2011) (from 2 to 22 Pg/yr, when ignoring the outliner at 118 Pg/yr). Our emitted mass below 10 μm is dominated by the emission of jet drops, given the shape of the distribution (see Figures 2 and 3).

The monthly mean maps in January and July show high productivity of salt is observed in the North Atlantic, North Pacific and the Southern Ocean corresponding to high wind and wave activity in winter time (shown in Supporting Information S1). We observe a strong seasonality in sea spray aerosol production in the Northern hemisphere storm track regions, contrasting the more persistent high production in the Southern hemisphere storm track regions.
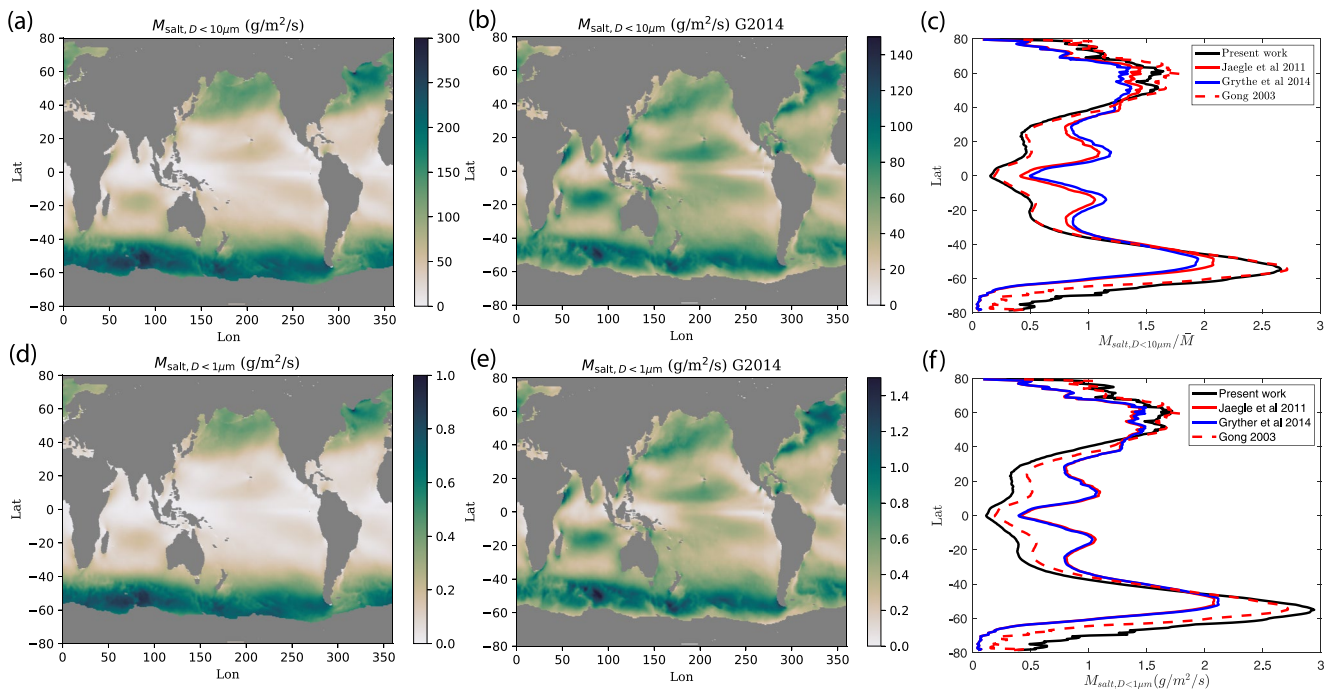
Figure 5. Annual mean distribution of sea salt emissions for $D_p < 10$ µm (first row) and $D_p < 1$ µm (second row) estimated from this study (panels a and d) and from the parameterization of Grythe et al. (2014) (panels b and e). Note that different color bar ranges are used in the different panels to highlight the regional patterns. The meridional distribution of annual sea salt emissions for each size range is summarized in panels (c and f) for our formulation for the same cut-offs, compared to Jaeglé et al. (2011), Grythe et al. (2014), and Gong (2003).

Figure 5d shows the emissions of sea salt emissions in the accumulation model (diameter smaller than 1 µm). Global emissions are of about 60 Tg/yr, similar to the value obtained using the empirical SSGF from Jaeglé et al. (2011) and Grythe et al. (2014) and discussed by Bian et al. (2019). It is remarkable that we obtain a value similar to previous estimates with our mechanistic approach. We comment again that our formulation tends to have more coarse mode relative to other parameterizations. Overall, these numbers are within the range discussed in de Leeuw et al. (2011) and Lewis and Schwartz (2004), and compatible with a more recent empirical formulation including sea state (Ovadnevaite et al., 2014).

Figures 5c and 5f show the normalized meridional distribution of sea spray emission with $D_p < 10$ µm and $D_p < 1$ µm, respectively. The spatial pattern generated by our formulation is very similar to that produced by the widely used Gong (2003) parameterization. This is in spite of the stronger dependency in wind speed assumed by Gong (2003) (based on Monahan and Muircheartaigh [1980] and reflects the impact of the sea state in our parameterization). In contrast, the Grythe et al. (2014) parameterization exhibits higher emissions in the tropics and lower emissions at high latitude. This reflects the strong modulation of the sea spray source function by SST derived from field observations (see also Jaeglé et al., 2011).

We comment that the spray of various sizes have different temperature sensitivity in our formulation (see Figure 2 which illustrates the sensitivity to temperature for each mechanism). In any of these cases, the temperature sensitivity coming from the proposed scalings is weaker than the one empirically derived by Jaeglé et al. (2011), yielding the zonal profiles in Figures 5c and 5f. This might suggest that some temperature dependent physics is missing in our formulation, and could come in a bursting efficiency parameter.

5. Discussion

We have presented a theoretical framework for sea spray aerosol production, building in recent advances in our understanding and modeling of sea spray production by bubble bursting, bubble entrainment by breaking waves, and breaking statistics. The final sea spray source function depends on temperature, through the role of water viscosity on production. The modes of production are described as scaling laws depending on the bubble bursting

radius and physical properties of water, based on physical arguments and evaluated against experiments on single bubble bursting, and include jet and film drops (film drops being decomposed into two modes of production). By convoluting these scaling laws with the typical bubble size distribution under a breaking wave, we obtain the sea spray production by bubble bursting, composed of the sum of the three modes of production. The peaks of production are radius (at 80% relative humidity) close to 100 nm and slightly below 1 μm for film drops, and about 2 μm for jet drops, with the radius increasing with water temperature. Next, the drop size distributions by bubble bursting are upscaled by considering the breaking statistics (represented by the length of breaking crest) and associated air entrained by breaking waves. The obtained volume of air entrained is an analog to the whitecap coverage and depends on wind speed and sea state, with increase of the entrained air at the same wind speed of up to a factor of 4 due to wave history. Our approach assumes proportionality between the number of entrained bubbles and the bubbles bursting efficiently and describe the processes in the mean sense, keeping in mind that each process presents an inherent statistical variability. We test the physics based sea spray generation function using output from a global wave model forced by realistic winds and results compare well with existing formulations in terms of wind speed dependency (see Figure 4), size distribution, and total amount of emitted sea salt in various size ranges. We also demonstrate the effect of the wave history in modulating the sea spray production, with variation in number of drops of up to a factor of 4 at a given wind speed.

We have presented an ocean spray emission function due to bubble bursting. To compare with volumetric aerosol size distribution in the atmosphere, we would need to consider the size dependent transport of the aerosols. The distribution of aerosols at a certain height in the atmosphere will depend on the residence time and settling velocity, which will be function of relative humidity, temperature and turbulence and affect the shape of the size distribution.

The present approach presents similarities with the classic bubble method (see Lewis & Schwartz, 2004; J. Wu, 1992), with two main conceptual differences. First, we have a direct estimate of air entrainment via the breaking statistics (following Deike et al. [2017]) and the volume flux of bubbles is obtained from wave modeling, while the bubble method relies on whitecap coverage with an empirical pre-factor tuned to a particular data set. We note that the volume flux of bubbles being entrained is not adjusted (and is consistent with work on bubble mediated gas transfer [see Deike & Melville, 2018]). Second, the quantification of aerosols differs when estimated as an ensemble of bubbles bursting. We consider scaling relationships describing the number and sizes of aerosols from individual bubble bursting experiments and integrate over the bubble size distribution measured under breaking waves to obtain the aerosol size distribution from bubble bursting (with the assumption that bubbles burst collectively as they would individually). In contrast, the bubble method uses the aerosol size distribution emitted in laboratory experiments where a particular bubble size distribution is generated to mimic bubbles entrained under a breaking wave.

An overall uncertainty in our proposed theoretical approach can be evaluated by considering the uncertainties on the various scaling relationships. The number of drops emitted by individual bubble bursting events can be considered known within a factor of 2, similarly to the total volume of entrained air by breaking waves in laboratory experiments. Air entrainment in the field would present uncertainties (similarly to the uncertainties in the whitecap coverage), but the sensitivity of the wave model to its numerical parameters (including grid resolution, frequency resolution, wind product, sensitivity to source terms in the spectral model) is smaller than the uncertainty in the above mentioned scaling relationships. Testing sensitivity to the range of uncertainties leads a global uncertainty of a factor of 3–5 on the final sea spray generation function. As stated above, we demonstrate that wave history can induce variations of up to a factor of 4 in the sea spray emissions, which explains some of the scatter reported in observational data set. Improving our ability to quantify wind wave effects can allow to focus the influence of other physical parameters. In particular, there are open questions on hygroscopic growth when going from size at emission to size of the resulting sea salt particles, as well as assumptions on collective effects and the role of temperature.

Large uncertainties remain on the role of temperature on sea spray aerosol production. Our scaling description of the mechanisms of production show a sensitivity to temperature on the number and radius of drops emitted by bursting, with each process affected in different ways (see Figure 1). Jet drop production is mainly modulated by temperature through its influence on viscosity, which controls the focusing of capillary waves that leads to an ascending jet. This results in larger drops at higher temperature, and overall fewer drops at higher temperature. Film drop production is also modulated by the effect of temperature through viscosity and Marangoni effect by

controlling the typical film thickness at bursting h_b, which itself controls the size and number of drops (with different relationships for mode I and mode II). This leads to larger drops with increasing temperature in all cases as the films tend to be thicker. The number of drops for film drop mode II (in the sub-micron regime, the newly proposed flapping mechanism) is expected to increase with temperature as it also scales with film thickness (while the number of supermicron film drop mode I is expected to decrease with temperature). As mentioned earlier, we do not account for the role of temperature on collective bursting, or bursting efficiency which remain to be assessed. Such effects might explain why our sensitivity to temperature is weaker than those empirically derived from observational data (Grythe et al., 2014; Saliba et al., 2019).

The prediction of smaller drops in colder water is in qualitative agreement with various field measurements (Saliba et al., 2019; Salter et al., 2015) and laboratory measurements (Mårtensson et al., 2003; Sellegri et al., 2006). The role of temperature on the total number of emitted sea spray aerosol is largely debated (Christiansen et al., 2019; Forestieri et al., 2018; Salter et al., 2014). Experiments with a plunging jet falling in water show an increase in surface bubble population with decreasing temperature leading to an increase in droplet population (Salter et al., 2014); while in other bubble production setup, the opposite effect was observed (Forestieri et al., 2018; Sellegri et al., 2006); but we have seen that air entrainment in the field does not seem sensitive to temperature (see Figure 2, as well as earlier discussion by Lewis and Schwartz [2004]). Recent field measurements tend to show an increase in the sea spray aerosol concentration with temperature (Grythe et al., 2014; Saliba et al., 2019), which would be consistent with the scaling proposed for the number of sub-micron aerosols. However, describing an increase in supermicron number of particles would require a modification in the production scaling. Such modification could come from collective effects controlled by temperature, and more generally an efficiency of bursting modulated by temperature that remain to be properly assessed. Similarly, the effect of surface contamination could be included in such efficiency factor. The production of organic aerosol could be modeled within the present framework, leveraging the separation of the different modes of production.

We conclude by emphasizing the applicability of the proposed physics-based formulation for sea spray aerosol emissions using wave models. This approach is in synergy with current efforts by several modeling centers to develop coupled oceanic and atmospheric wave models (e.g., Couvelard et al., 2020; Li et al., 2016; L. Wu et al., 2019), moving toward coupled wave-atmosphere-ocean Earth system models.

Conflict of Interest

The authors declare no conflicts of interest relevant to this study.

Data Availability Statement

NOAA High Resolution SST data provided by the NOAA/OAR/ESRL PSL, Boulder, Colorado, USA, from their Web site at: https://psl.noaa.gov/data/gridded/data.noaa.oisst.v2.highres.html. The WAVEWATCH-III model is available at: https://github.com/NOAA-EMC/WW3. We thank Leonel Romero for discussion on modeling the breaking distribution within WW3. The WAVEWATCH-III model with the Romero (2019) formulation for breaking distribution, whitecap coverage and volume of air entrained is available at: https://github.com/Leonel-Romero/WW3-Lambda. The statements, findings, conclusions, and recommendations are those of the author(s) and do not necessarily reflect the views of the National Oceanic and Atmospheric Administration, or the U.S. Department of Commerce.

References

Adcroft, A., Anderson, W., Balaji, V., Blanton, C., Bushuk, M., Dufour, C. O., et al. (2019). The GFDL global ocean and sea ice model OM4. 0: Model description and simulation features. *Journal of Advances in Modeling Earth Systems*, *11*(10), 3167–3211. https://doi.org/10.1029/2019ms001726

Aliseda, A., & Lasheras, J. (2011). Preferential concentration and rise velocity reduction of bubbles immersed in a homogeneous and isotropic turbulent flow. *Physics of Fluids*, *23*(9), 093301. https://doi.org/10.1063/1.3626404

Ardhuin, F., Rogers, E., Babanin, A. V., Filipot, J.-F., Magne, R., Roland, A., et al. (2010). Semiempirical dissipation source functions for ocean waves. Part I: Definition, calibration, and validation. *Journal of Physical Oceanography*, *40*(9), 1917–1941. https://doi.org/10.1175/2010jpo4324.1

Bell, T. G., Landwehr, S., Miller, S. D., Bruyn, W. J., Callaghan, A. H., Scanlon, B., et al. (2017). Estimation of bubble-mediated air–sea gas exchange from concurrent DMS and CO_2 transfer velocities at intermediate–high wind speeds. *Atmospheric Chemistry and Physics*, *17*(14), 9019–9033. https://doi.org/10.5194/acp-17-9019-2017

Berny, A., Deike, L., Séon, T., & Popinet, S. (2020). Role of all jet drops in mass transfer from bursting bubbles. *Physical Review Fluids*, *5*(3), 033605. https://doi.org/10.1103/physrevfluids.5.033605

Berny, A., Popinet, S., Séon, T., & Deike, L. (2021). Statistics of jet drop production. *Geophysical Research Letters*, *48*(10), e2021GL092919. https://doi.org/10.1029/2021gl092919

Bertram, T. H., Cochran, R. E., Grassian, V. H., & Stone, E. A. (2018). Sea spray aerosol chemical composition: Elemental and molecular mimics for laboratory studies of heterogeneous and multiphase reactions. *Chemical Society Reviews*, *47*(7), 2374–2400. https://doi.org/10.1039/c7cs00008a

Bian, H., Froyd, K., Murphy, D. M., Dibb, J., Darmenov, A., Chin, M., et al. (2019). Observationally constrained analysis of sea salt aerosol in the marine atmosphere. *Atmospheric Chemistry and Physics*, *19*(16), 10773–10785. https://doi.org/10.5194/acp-19-10773-2019

Blanchard, D. C. (1963). The electrification of the atmosphere by particles from bubbles in the sea. *Progress in Oceanography*, *1*, 73–112, IN7, 113–202. https://doi.org/10.1016/0079-6611(63)90004-1

Blanchard, D. C. (1989). The size and height to which jet drops are ejected from bursting bubbles in seawater. *Journal of Geophysical Research*, *94*(C8), 10999–11002. https://doi.org/10.1029/jc094ic08p10999

Blanchard, D. C., & Syzdek, L. D. (1988). Film drop production as a function of bubble size. *Journal of Geophysical Research*, *93*(C4), 3649–3654. https://doi.org/10.1029/jc093ic04p03649

Blanchard, D. C., & Woodcock, A. H. (1957). Bubble formation and modification in the sea and its meteorological significance. *Tellus*, *9*(2), 145–158. https://doi.org/10.1111/j.2153-3490.1957.tb01867.x

Blenkinsopp, C. E., & Chaplin, J. R. (2010). Bubble size measurements in breaking waves using optical fiber phase detection probes. *IEEE Journal of Oceanic Engineering*, *35*(2), 388–401. https://doi.org/10.1109/joe.2010.2044940

Brasz, C. F., Bartlett, C. T., Walls, P. L. L., Flynn, E. G., Yu, Y. E., & Bird, J. C. (2018). Minimum size for the top jet drop from a bursting bubble. *Physical Review Fluids*, *3*(7), 074001. https://doi.org/10.1103/PhysRevFluids.3.074001

Brumer, S., Zappa, C., Blomquist, B., Fairall, C., Cifuentes-Lorenzen, A., Edson, J., et al. (2017). Wave-related Reynolds number parameterizations of CO_2 and DMS transfer velocities. *Geophysical Research Letters*, *44*(19), 9865–9875. https://doi.org/10.1002/2017gl074979

Callaghan, A., de Leeuw, G., Cohen, L., & O'Dowd, C. (2008). Relationship of oceanic whitecap coverage to wind speed and wind history. *Geophysical Research Letters*, *35*(23), L23609. https://doi.org/10.1029/2008gl036165

Callaghan, A. H., Stokes, M., & Deane, G. (2014). The effect of water temperature on air entrainment, bubble plumes, and surface foam in a laboratory breaking-wave analog. *Journal of Geophysical Research: Oceans*, *119*(11), 7463–7482. https://doi.org/10.1002/2014jc010351

Chawla, A., Spindler, D. M., & Tolman, H. L. (2013). Validation of a thirty year wave hindcast using the climate forecast system reanalysis winds. *Ocean Modelling*, *70*, 189–206. https://doi.org/10.1016/j.ocemod.2012.07.005

Christiansen, S., Salter, M. E., Gorokhova, E., Nguyen, Q. T., & Bilde, M. (2019). Sea spray aerosol formation: Laboratory results on the role of air entrainment, water temperature, and phytoplankton biomass. *Environmental Science & Technology*, *53*(22), 13107–13116. https://doi.org/10.1021/acs.est.9b04078

Cipriano, R. J., & Blanchard, D. C. (1981). Bubble and aerosol spectra produced by a laboratory 'breaking wave'. *Journal of Geophysical Research*, *86*(C9), 8085–8092. https://doi.org/10.1029/jc086ic09p08085

Cochran, R. E., Ryder, O. S., Grassian, V. H., & Prather, K. A. (2017). Sea spray aerosol: The chemical link between the oceans, atmosphere, and climate. *Accounts of Chemical Research*, *50*(3), 599–604. https://doi.org/10.1021/acs.accounts.6b00603

Couvelard, X., Lemarié, F., Samson, G., Redelsperger, J.-L., Ardhuin, F., Benshila, R., & Madec, G. (2020). Development of a two-way-coupled ocean–wave model: Assessment on a global NEMO (v3.6)–WW3 (v6.02) coupled configuration. *Geoscientific Model Development*, *13*(7), 3067–3090. https://doi.org/10.5194/gmd-13-3067-2020

Czerski, H., Brooks, I. M., Gunn, S., Pascal, R., Matei, A., & Blomquist, B. (2022a). Ocean bubbles under high wind conditions–Part 1: Bubble distribution and development. *Ocean Science*, *18*(3), 565–586. https://doi.org/10.5194/os-18-565-2022

Czerski, H., Brooks, I. M., Gunn, S., Pascal, R., Matei, A., & Blomquist, B. (2022b). Ocean bubbles under high wind conditions–Part 2: Bubble size distributions and implications for models of bubble dynamics. *Ocean Science*, *18*(3), 587–608. https://doi.org/10.5194/os-18-587-2022

Deane, G. B., & Stokes, M. D. (2002). Scale dependence of bubble creation mechanisms in breaking waves. *Nature*, *418*(6900), 839–844. https://doi.org/10.1038/nature00967

Deike, L. (2022). Mass transfer at the ocean–atmosphere interface: The role of wave breaking, droplets, and bubbles. *Annual Review of Fluid Mechanics*, *54*(1), 191–224. https://doi.org/10.1146/annurev-fluid-030121-014132

Deike, L., Ghabache, E., Liger-Belair, G., Das, A. K., Zaleski, S., Popinet, S., & Seon, T. (2018). The dynamics of jets produced by bursting bubbles. *Physical Review Fluids*, *3*(1), 013603. https://doi.org/10.1103/physrevfluids.3.013603

Deike, L., Lenain, L., & Melville, W. K. (2017). Air entrainment by breaking waves. *Geophysical Research Letters*, *44*(8), 3779–3787. https://doi.org/10.1002/2017gl072883

Deike, L., Melville, W., & Popinet, S. (2016). Air entrainment and bubble statistics in breaking waves. *Journal of Fluid Mechanics*, *801*, 91–129. https://doi.org/10.1017/jfm.2016.372

Deike, L., & Melville, W. K. (2018). Gas transfer by breaking waves. *Geophysical Research Letters*, *45*(19), 10–482. https://doi.org/10.1029/2018gl078758

de Leeuw, G., Andreas, E. L., Anguelova, M. D., Fairall, C. W., Lewis, E. R., O'Dowd, C., et al. (2011). Production flux of sea spray aerosol. *Reviews of Geophysics*, *49*(2), RG2001. https://doi.org/10.1029/2010rg000349

DeMott, P. J., Hill, T. C., McCluskey, C. S., Prather, K. A., Collins, D. B., Sullivan, R. C., et al. (2016). Sea spray aerosol as a unique source of ice nucleating particles. *Proceedings of the National Academy of Sciences*, *113*(21), 5797–5803. https://doi.org/10.1073/pnas.1514034112

Drazen, D. A., Melville, W. K., & Lenain, L. (2008). Inertial scaling of dissipation in unsteady breaking waves. *Journal of Fluid Mechanics*, *611*(1), 307–332. https://doi.org/10.1017/s0022112008002826

Fitzgerald, J. W. (1975). Approximation formulas for the equilibrium size of an aerosol particle as a function of its dry size and composition and the ambient relative humidity. *Journal of Applied Meteorology and Climatology*, *14*(6), 1044–1049. https://doi.org/10.1175/1520-0450(1975)014<1044:afftes>2.0.co;2

Forestieri, S., Moore, K., Martinez Borrero, R., Wang, A., Stokes, M., & Cappa, C. (2018). Temperature and composition dependence of sea spray aerosol production. *Geophysical Research Letters*, *45*(14), 7218–7225. https://doi.org/10.1029/2018gl078193

Gañán-Calvo, A. M. (2017). Revision of bubble bursting: Universal scaling laws of top jet drop size and speed. *Physical Review Letters*, *119*(20), 204502. https://doi.org/10.1103/physrevlett.119.204502

Ghabache, E. (2015). Surface libre hors équilibre: De l'effondrement de cavité aux jets étirés (Unpublished doctoral dissertation).

Ghabache, E., Antkowiak, A., Josserand, C., & Séon, T. (2014). On the physics of fizziness: How bubble bursting controls droplets ejection. *Physics of Fluids*, *26*(12), 121701. https://doi.org/10.1063/1.4902820

Ghabache, E., & Séon, T. (2016). Size of the top jet drop produced by bubble bursting. *Physical Review Fluids*, *1*(5), 051901. https://doi.org/10.1103/physrevfluids.1.051901

Gong, S. (2003). A parameterization of sea-salt aerosol source function for sub-and super-micron particles. *Global Biogeochemical Cycles*, *17*(4), 1097. https://doi.org/10.1029/2003gb002079

Grythe, H., Ström, J., Krejci, R., Quinn, P., & Stohl, A. (2014). A review of sea-spray aerosol source functions using a large global set of sea salt aerosol concentration measurements. *Atmospheric Chemistry and Physics*, *14*(3), 1277–1297. https://doi.org/10.5194/acp-14-1277-2014

Hayami, S., & Toba, Y. (1958). Drop production by bursting of air bubbles on the sea surface (1) experiments at still sea water surface. *Journal of the Oceanographical Society of Japan*, *14*(4), 145–150. https://doi.org/10.5928/kaiyou1942.14.145

Hinze, J. O. (1955). Fundamentals of the hydrodynamic mechanism of splitting in dispersion processes. *AIChE Journal*, *1*(3), 289–295. https://doi.org/10.1002/aic.690010303

Jaeglé, L., Quinn, P., Bates, T., Alexander, B., & Lin, J.-T. (2011). Global distribution of sea salt aerosols: New constraints from in situ and remote sensing observations. *Atmospheric Chemistry and Physics*, *11*(7), 3137–3157. https://doi.org/10.5194/acp-11-3137-2011

Janssen, P., & Janssen, P. A. (2004). *The interaction of ocean waves and wind*. Cambridge University Press.

Jiang, X., Rotily, L., Villermaux, E., & Wang, X. (2022). Submicron drops from flapping bursting bubbles. *Proceedings of the National Academy of Sciences*, *119*(1), e2112924119. https://doi.org/10.1073/pnas.2112924119

Johnson, J. S., Regayre, L. A., Yoshioka, M., Pringle, K. J., Turnock, S. T., Sexton, D. M., et al. (2020). Robust observational constraint of uncertain aerosol processes and emissions in a climate model and the effect on aerosol radiative forcing. *Atmospheric Chemistry and Physics*, *20*(15), 9491–9524. https://doi.org/10.5194/acp-20-9491-2020

Kleiss, J. M., & Melville, W. K. (2010). Observations of wave breaking kinematics in fetch-limited seas. *Journal of Physical Oceanography*, *40*(12), 2575–2604. https://doi.org/10.1175/2010jpo4383.1

Kobayashi, S., Ota, Y., Harada, Y., Ebita, A., Moriya, M., Onoda, H., et al. (2015). The JRA-55 reanalysis: General specifications and basic characteristics. *Journal of the Meteorological Society of Japan. Ser. II*, *93*(1), 5–48. https://doi.org/10.2151/jmsj.2015-001

Komen, G. J., Cavaleri, L., Donelan, M., Hasselmann, K., Hasselmann, S., & Janssen, P. (1996). Dynamics and modelling of ocean waves.

Lamarre, E., & Melville, W. (1991). Air entrainment and dissipation in breaking waves. *Nature*, *351*(6326), 469–472. https://doi.org/10.1038/351469a0

Lewis, E. R., & Schwartz, S. E. (2004). *Sea salt aerosol production. mechanisms, methods, measurements, and models. Geophysical Monograph* (Vol. 152). American Geophysical Union.

Lhuissier, H., & Villermaux, E. (2012). Bursting bubble aerosols. *Journal of Fluid Mechanics*, *696*, 5–44. https://doi.org/10.1017/jfm.2011.418

Li, Q., Webb, A., Fox-Kemper, B., Craig, A., Danabasoglu, G., Large, W. G., & Vertenstein, M. (2016). Langmuir mixing effects on global climate: WAVEWATCH III in CESM. *Ocean Modelling*, *103*, 145–160. (Waves and coastal, regional and global processes). https://doi.org/10.1016/j.ocemod.2015.07.020

Liu, S., Liu, C.-C., Froyd, K. D., Schill, G. P., Murphy, D. M., Bui, T. P., et al. (2021). Sea spray aerosol concentration modulated by sea surface temperature. *Proceedings of the National Academy of Sciences*, *118*(9), e2020583118. https://doi.org/10.1073/pnas.2020583118

Loewen, M. R., & Melville, W. K. (1994). An experimental investigation of the collective oscillations of bubble plumes entrained by breaking waves. *Journal of the Acoustical Society of America*, *95*(3), 1329–1343. https://doi.org/10.1121/1.408573

Mårtensson, E., Nilsson, E., de Leeuw, G., Cohen, L., & Hansson, H.-C. (2003). Laboratory simulations and parameterization of the primary marine aerosol production. *Journal of Geophysical Research*, *108*(D9), 4297. https://doi.org/10.1029/2002jd002263

Meskhidze, N., Petters, M. D., Tsigaridis, K., Bates, T., O'Dowd, C., Reid, J., et al. (2013). *Production mechanisms, number concentration, size distribution, chemical composition, and optical properties of sea spray aerosols*. Wiley Online Library.

Monahan, E. C., & Muircheartaigh, I. (1980). Optimal power-law description of oceanic whitecap coverage dependence on wind speed. *Journal of Physical Oceanography*, *10*(12), 2094–2099. https://doi.org/10.1175/1520-0485(1980)010<2094:opldoo>2.0.co;2

Moore, D., & Mason, B. (1954). The concentration, size distribution and production rate of large salt nuclei over the oceans. *Quarterly Journal of the Royal Meteorological Society*, *80*(346), 583–590. https://doi.org/10.1002/qj.49708034607

Mostert, W., Popinet, S., & Deike, L. (2022). High-resolution direct simulation of deep water breaking waves: Transition to turbulence, bubbles and droplet production. *Journal of Fluid Mechanics*, *942*, A27. https://doi.org/10.1017/jfm.2022.330

Néel, B., & Deike, L. (2021). Collective bursting of free-surface bubbles, and the role of surface contamination. *Journal of Fluid Mechanics*, *917*. https://doi.org/10.1017/jfm.2021.272

Neel, B., Erinin, M., & Deike, L. (2022). Role of contamination in optimal droplet production by collective bubble bursting. *Geophysical Research Letters*, *49*(1), e2021GL096740. https://doi.org/10.1029/2021gl096740

Ovadnevaite, J., Manders, A., De Leeuw, G., Ceburnis, D., Monahan, C., Partanen, A.-I., et al. (2014). A sea spray aerosol flux parameterization encapsulating wave state. *Atmospheric Chemistry and Physics*, *14*(4), 1837–1852. https://doi.org/10.5194/acp-14-1837-2014

Painemal, D., Minnis, P., & Nordeen, M. (2015). Aerosol variability, synoptic-scale processes, and their link to the cloud microphysics over the northeast Pacific during MAGIC. *Journal of Geophysical Research: Atmospheres*, *120*(10), 5122–5139. https://doi.org/10.1002/2015jd023175

Paulot, F., Paynter, D., Winton, M., Ginoux, P., Zhao, M., & Horowitz, L. W. (2020). Revisiting the impact of sea salt on climate sensitivity. *Geophysical Research Letters*, *47*(3), e2019GL085601. https://doi.org/10.1029/2019gl085601

Phillips, O. (1985). Spectral and statistical properties of the equilibrium range in wind-generated gravity waves. *Journal of Fluid Mechanics*, *156*(1), 505–531. https://doi.org/10.1017/s0022112085002221

Poulain, S., Villermaux, E., & Bourouiba, L. (2018). Ageing and burst of surface bubbles. *Journal of Fluid Mechanics*, *851*, 636–671. https://doi.org/10.1017/jfm.2018.471

Prather, K. A., Bertram, T. H., Grassian, V. H., Deane, G. B., Stokes, M. D., DeMott, P. J., et al. (2013). Bringing the ocean into the laboratory to probe the chemical complexity of sea spray aerosol. *Proceedings of the National Academy of Sciences*, *110*(19), 7550–7555. https://doi.org/10.1073/pnas.1300262110

Quinn, P. K., Collins, D. B., Grassian, V. H., Prather, K. A., & Bates, T. S. (2015). Chemistry and related properties of freshly emitted sea spray aerosol. *Chemical Reviews*, *115*(10), 4383–4399. https://doi.org/10.1021/cr500713g

Reichl, B. G., & Deike, L. (2020). Contribution of sea-state dependent bubbles to air-sea carbon dioxide fluxes. *Geophysical Research Letters*, *47*(9), e2020GL087267. https://doi.org/10.1029/2020gl087267

Resch, F., & Afeti, G. (1991). Film drop distributions from bubbles bursting in seawater. *Journal of Geophysical Research*, *96*(C6), 10681–10688. https://doi.org/10.1029/91jc00433

Reynolds, R. W., Smith, T. M., Liu, C., Chelton, D. B., Casey, K. S., & Schlax, M. G. (2007). Daily high-resolution-blended analyses for sea surface temperature. *Journal of Climate*, *20*(22), 5473–5496. https://doi.org/10.1175/2007JCLI1824.1

Richter, D. H., Dempsey, A. E., & Sullivan, P. P. (2019). Turbulent transport of spray droplets in the vicinity of moving surface waves. *Journal of Physical Oceanography*, *49*(7), 1789–1807. https://doi.org/10.1175/jpo-d-19-0003.1

Rivière, A., Mostert, W., Perrard, S., & Deike, L. (2021). Sub-hinze scale bubble production in turbulent bubble break-up. *Journal of Fluid Mechanics*, *917*. https://doi.org/10.1017/jfm.2021.243

Rivière, A., Ruth, D., Mostert, W., Deike, L., & Perrard, S. (2022). Capillary driven fragmentation of large gas bubbles in turbulence. *Physical Review Fluids*, *7*(8), 083602. https://doi.org/10.1103/physrevfluids.7.083602

Rojas, G., & Loewen, M. (2007). Fiber-optic probe measurements of void fraction and bubble size distributions beneath breaking waves. *Experiments in Fluids*, *43*(6), 895–906. https://doi.org/10.1007/s00348-007-0356-5

Romero, L. (2019). Distribution of surface wave breaking fronts. *Geophysical Research Letters*, *46*(17–18), 10463–10474. https://doi.org/10.1029/2019gl083408

Romero, L., Melville, W. K., & Kleiss, J. M. (2012). Spectral energy dissipation due to surface wave breaking. *Journal of Physical Oceanography*, *42*(9), 1421–1441. https://doi.org/10.1175/jpo-d-11-072.1

Saliba, G., Chen, C.-L., Lewis, S., Russell, L. M., Rivellini, L.-H., Lee, A. K., et al. (2019). Factors driving the seasonal and hourly variability of sea-spray aerosol number in the North Atlantic. *Proceedings of the National Academy of Sciences*, *116*(41), 20309–20314. https://doi.org/10.1073/pnas.1907574116

Salter, M. E., Nilsson, E. D., Butcher, A., & Bilde, M. (2014). On the seawater temperature dependence of the sea spray aerosol generated by a continuous plunging jet. *Journal of Geophysical Research: Atmospheres*, *119*(14), 9052–9072. https://doi.org/10.1002/2013jd021376

Salter, M. E., Zieger, P., Acosta Navarro, J. C., Grythe, H., Kirkevåg, A., Rosati, B., et al. (2015). An empirically derived inorganic sea spray source function incorporating sea surface temperature. *Atmospheric Chemistry and Physics*, *15*(19), 11047–11066. https://doi.org/10.5194/acp-15-11047-2015

Schwendeman, M., & Thomson, J. (2015). Observations of whitecap coverage and the relation to wind stress, wave slope, and turbulent dissipation. *Journal of Geophysical Research: Oceans*, *120*(12), 8346–8363. https://doi.org/10.1002/2015jc011196

Sellegri, K., O'Dowd, C., Yoon, Y., Jennings, S., & de Leeuw, G. (2006). Surfactants and submicron sea spray generation. *Journal of Geophysical Research*, *111*(D22), D22215. https://doi.org/10.1029/2005jd006658

Shaw, D., & Deike, L. (2022). Bubble bursting for various water conditions. In preparation.

Spiel, D. E. (1994). The number and size of jet drops produced by air bubbles bursting on a fresh water surface. *Journal of Geophysical Research*, *99*(C5), 10289–10296. https://doi.org/10.1029/94jc00382

Spiel, D. E. (1997). More on the births of jet drops from bubbles bursting on seawater surfaces. *Journal of Geophysical Research*, *102*(C3), 5815–5821. https://doi.org/10.1029/96jc03582

Spiel, D. E. (1998). On the births of film drops from bubbles bursting on seawater surfaces. *Journal of Geophysical Research*, *103*(C11), 24907–24918. https://doi.org/10.1029/98jc02233

Sutherland, P., & Melville, W. K. (2013). Field measurements and scaling of ocean surface wave-breaking statistics. *Geophysical Research Letters*, *40*(12), 3074–3079. https://doi.org/10.1002/grl.50584

Thorpe, S. (1982). On the clouds of bubbles formed by breaking wind-waves in deep water, and their role in air–sea gas transfer. *Philosophical Transactions of the Royal Society of London A: Mathematical, Physical and Engineering Sciences*, *304*(1483), 155–210.

Tsujino, H., Urakawa, S., Nakano, H., Small, R. J., Kim, W. M., Yeager, S. G., et al. (2018). JRA-55 based surface dataset for driving ocean–sea-ice models (JRA55-do). *Ocean Modelling*, *130*, 79–139. https://doi.org/10.1016/j.ocemod.2018.07.002

Veron, F. (2015). Ocean spray. *Annual Review of Fluid Mechanics*, *47*(1), 507–538. https://doi.org/10.1146/annurev-fluid-010814-014651

Villermaux, E. (2020). Fragmentation versus cohesion. *Journal of Fluid Mechanics*, *898*. https://doi.org/10.1017/jfm.2020.366

Walls, P., Henaux, L., & Bird, J. C. (2015). Jet drops from bursting bubbles: How gravity and viscosity couple to inhibit droplet production. *Physics Reviews*, *92*(2), 021002. https://doi.org/10.1103/physreve.92.021002

Wang, J., Wood, R., Jensen, M. P., Chiu, J. C., Liu, Y., Lamer, K., et al. (2021). Aerosol and cloud experiments in the eastern North Atlantic (ACE-ENA). *Bulletin of the American Meteorological Society*, *103*(2), 1–51. https://doi.org/10.1175/bams-d-19-0220.1

Wang, X., Deane, G. B., Moore, K. A., Ryder, O. S., Stokes, M. D., Beall, C. M., et al. (2017). The role of jet and film drops in controlling the mixing state of submicron sea spray aerosol particles. *Proceedings of the National Academy of Sciences*, *114*(27), 6978–6983. https://doi.org/10.1073/pnas.1702420114

Wang, Z., Yang, J., & Stern, F. (2016). High-fidelity simulations of bubble, droplet and spray formation in breaking waves. *Journal of Fluid Mechanics*, *792*, 307–327. https://doi.org/10.1017/jfm.2016.87

Woolf, D. K., & Thorpe, S. (1991). Bubbles and the air-sea exchange of gases in near-saturation conditions. *Journal of Marine Research*, *49*(3), 435–466. https://doi.org/10.1357/002224091784995765

Wu, J. (1992). Bubble flux and marine aerosol spectra under various wind velocities. *Journal of Geophysical Research*, *97*(C2), 2327–2333. https://doi.org/10.1029/91jc02568

Wu, L., Breivik, O., & Rutgersson, A. (2019). Ocean-wave-atmosphere interaction processes in a fully coupled modeling system. *Journal of Advances in Modeling Earth Systems*, *11*(11), 3852–3874. https://doi.org/10.1029/2019MS001761

WW3DG. (2016). *User manual and system documentation of WAVEWATCH III version 5.16*. (Technical Report). NOAA/NWS/NCEP/MMAB.

Zappa, C. J., Banner, M., Schultz, H., Gemmrich, J., Morison, R., LeBel, D., & Dickey, T. (2012). An overview of sea state conditions and air-sea fluxes during RaDyO. *Journal of Geophysical Research*, *117*(C7). https://doi.org/10.1029/2011jc007336

Zieger, P., Väisänen, O., Corbin, J. C., Partridge, D. G., Bastelberger, S., Mousavi-Fard, M., et al. (2017). Revising the hygroscopicity of inorganic sea salt particles. *Nature Communications*, *8*(1), 1–10. https://doi.org/10.1038/ncomms15883